ECCOMAS Congress 2016
VII European Congress on Computational Methods in Applied Sciences and Engineering
M. Papadrakakis, V. Papadopoulos, G. Stefanou, V. Plevris (eds.)
Crete Island, Greece, 5–10 June 2016

ISOTROPY–PRESERVING SLOPE LIMITERS FOR FINITE VOLUME METHODS ON SQUARE MESHES

J. Velechovsky[1] **and M. M. Francois**[1]

[1]Los Alamos National Laboratory
Los Alamos, NM 87544, USA
e-mail: {jan,mmfran}@lanl.gov

Keywords: Slope limiter, isotropic numerical scheme, symmetry preserving numerical scheme, finite volume method, directional split, MUSCL–Hancock.

Abstract. *Directional split is a common technique used in Finite–Volume Methods (FVM) for solving multidimensional hyperbolic partial differential equations on regular grids. The directional split method is based on independent one–dimensional flux calculation for each Cartesian direction. Second order accuracy is achieved by doing a piecewise linear calculation of cell quantities in a Monotonic Upstream–Centered Scheme for Conservation Laws (MUSCL) scheme. This one–dimensional reconstruction results in artificial grid–orientation dependence of the numerical solution, i.e. some anisotropy are introduced even for originally isotropic problems. To mitigate the anisotropy of these schemes we propose to use extended two–dimensional stencils during the reconstruction step, while keeping the directional–split nature of the scheme.*

In this work, we introduce a novel multi–dimensional modification of the minmod slope limiter in the context of a MUSCL Hancock directional split FVM numerical scheme. Local direction of the unlimited gradient is utilized in the construction of our limiter. Improvements in the isotropy of the numerical solution are demonstrated for the linear advection as well as for standard hydrodynamics test cases on square meshes.

1 INTRODUCTION

In Finite–Volume Methods (FVM), second–order accuracy is achieved by using piecewise linear reconstruction of the variable quantities [1]. Near discontinuities, the most important part of the reconstruction is to reduce (limit) calculated slopes. This limitation is typically enforced by a slope limiter. FVM schemes traditionally employ directional split on regular grids. Consequently, the piecewise linear reconstruction is typically constructed independently for each Cartesian direction. Such directional one–dimensional reconstruction has for effect to introduce artificial anisotropy error in the numerical solution. The goal of this paper is to analyze and mitigate this numerical anisotropy error.

For hydrodynamic problems with a smooth solution, isotropic finite–difference scheme such as in [2] can be employed. The scheme is free of the directional (anisotropic) error in error terms of the lowest order. To approximate the first derivative, these isotropic finite–differences are based on six–point stencil in two spatial dimensions contrary to two–point (one–dimensional) stencil for the standard central difference approximation. Further theoretical analysis and the derivation of an isotropic finite volume discretization was presented in [3].

For a discontinuous solution, necessary constraints to avoid a numerical oscillation during the application of slope limiters on square meshes were derived in [4]. These additional constraints for one–dimensional Total Variation Disminishing (TVD) limiters are the main part of this Multi–dimensional Limiting Process (MLP). On unstructured grids, this MLP procedure reduces [5] to the classical multi–dimensional Barth–Jespersen limiter [6] with an extended stencil. A multi–dimensional application of slope limiters on unstructured grids with particular interest to definition of maximum principle regions was reviewed in [7]. An alternative approach to direct reconstruction limiting using Vector Image Polygon for scalar variables was presented in [8].

In this paper, we examine the standard one–dimensional minmod limiter [9] for a piecewise linear reconstruction. On a set of numerical examples, we demonstrate the development of an artificial anisotropy, which is introduced by this limiter. We propose a novel multi–dimensional extension of the minmod limiter to mitigate this anisotropy. This is in contrast to MLP and another approaches, where the original minmod limiter satisfies all multi–dimensional requirements.

The paper is organized as follows. A review of a directional split MUSCL Hancock numerical discretization [1] of the Euler equations is provided in next section. The third section is devoted to the piecewise linear reconstruction and to the presentation of our novel multi–dimensional variations of the minmod limiter. These limiters are numerically investigated in section 4. At first, an analysis of convergence and symmetry preservation is provided for the linear advection. Performance of our multi–dimensional Principal limiter is further demonstrated for Sedov and Noh hydrodynamic test cases.

2 NUMERICAL DISCRETIZATION

In this work, we use a directional split MUSCL Hancock numerical scheme [1] to solve the Euler equations. The scheme is based on a sequential application of one–dimensional numerical method along main axes x and y. For every time–step Δt, we apply both updates in the x– and y–direction independently, whereas the order of the direction is alternated.

Here we provide a short review of the directional split MUSCL Hancock scheme employing a piece–wise linear reconstruction of primitive variables inside a computational domain. One–

dimensional piecewise linear reconstruction in each computational cell i has the form

$$\mathbf{W}^{\pm}{}_{i} = \mathbf{W}_i \pm \frac{\boldsymbol{\Delta}_i}{2}\,, \tag{1}$$

for $\mathbf{W} = (w, v, p, \rho)^T$ in the case of the two–dimensional Euler equations.

$$\boldsymbol{\Delta}_{\mathbf{i}} = \mathbf{W}_i^x \Delta x\,, \qquad\qquad \mathbf{W}_i^x = (w_i^x, v_i^x, p_i^x, \rho_i^x)^T\,. \tag{2}$$

These slope approximations $\mathbf{W}_i^x$ are determined by a slope limiter. Traditionally, the slope limiter is calculated independently using one–dimensional information. Different piecewise linear reconstructions using slope limiters are reviewed in section 3.

The first part of the scheme is the predictor step to the time–level $n + 1/2$. In the x–sweep, the system

$$\mathbf{W}_t + \mathbb{A}\mathbf{W}_x = \mathbf{0} \qquad \mathbb{A} = \begin{pmatrix} w & 0 & 1/\rho & 0 \\ 0 & w & 0 & 0 \\ \rho c^2 & 0 & w & 0 \\ \rho & 0 & 0 & w \end{pmatrix} \qquad \mathbf{W} = \begin{pmatrix} w \\ v \\ p \\ \rho \end{pmatrix} \tag{3}$$

with the sound speed c is solved explicitly in each computational cell i for the face extrapolated values

$$\mathbf{W}^{\pm}{}_{i}^{n+1/2} = \mathbf{W}^{\pm}{}_{i}^{n} - \frac{1}{2}\frac{\Delta t}{\Delta x}\mathbb{A}(\mathbf{W}^{\pm}{}_{i}^{n})\boldsymbol{\Delta}_i^n\,. \tag{4}$$

For these face extrapolated values, we apply the HLL Riemann solver [10] with wave speed approximations

$$S_L = \min(u_L - c_L, u_R - c_R) \tag{5}$$

$$S_R = \max(u_L + c_L, u_R + c_R)\,. \tag{6}$$

3 TWO–DIMENSIONAL PIECEWISE LINEAR RECONSTRUCTION

The general form of a piecewise linear reconstruction (preserving a mean quantity) inside a computational cell i, j is

$$u(x, y) = u_{i,j} + u_{i,j}^x(x - x_{i,j}) + u_{i,j}^y(y - y_{i,j})\,, \tag{7}$$

where $(x_{i,j}, y_{i,j})$ is the cell center coordinate and u is the quantity. On a square computational mesh, this reconstruction can be calculated independently for each orthogonal direction x and y assuming the location of inter–cell fluxes at centers of mesh faces as indicated in Figure 1. For faces aligned with the x axis, we can write

$$u_{i,j+1/2,L} = u_{i,j} + u_{i,j}^x(x_{i,j} - x_{i,j}) + u_{i,j}^y(y_{i,j} + \frac{\Delta x}{2} - y_{i,j}) = u_{i,j} + u_{i,j}^y\frac{\Delta x}{2} \tag{8}$$

and the application of one–dimensional slope limiters seems to be appropriate.

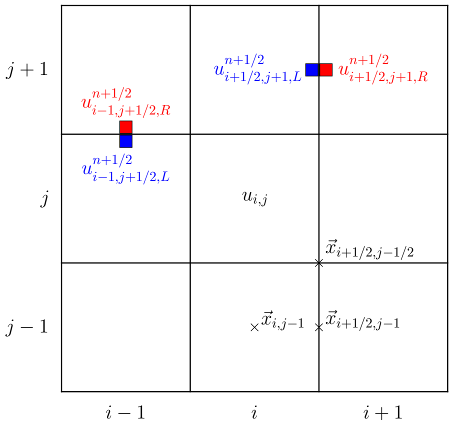

Figure 1: Computational mesh schematic. Cell coordinate and mean cell quantity $u_{i,j}$ shown in black. Left and right face–based reconstructed states shown in blue/red.

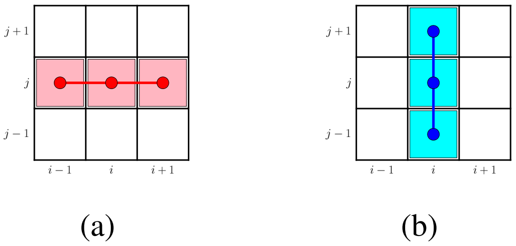

(a) (b)

Figure 2: Schematic representation of the MinMod reconstruction along split directions inside the central cell i, j. x–direction in (a) and y–direction in (b). Potential slopes indicated by "barbells". Effective cells emphasized in color.

3.1 One–dimensional mimmod limiter

The standard one–dimensional mimmod (1D MinMod) limiter for a piecewise linear reconstruction uses only the information along one direction. Here, we present the formulas only for x–direction. Assuming the mean value $u_i = u_{i,j}$ (for fixed j) in the cell i, we compute limited slopes as a combination of the left $u_i^{x,L} = \frac{u_i - u_{i-1}}{\Delta x}$ and the right $u_i^{x,R} = \frac{u_{i+1} - u_i}{\Delta x}$ finite difference approximations using the minmod function to get the final slope

$$u_i^{x,\text{minmod}} = \begin{cases} 0 & \text{if} \quad u_i^{x,L} u_i^{x,R} < 0 \\ \text{sign}(u_i^{x,L}) \min(|u_i^{x,L}|, |u_i^{x,R}|) & \text{else.} \end{cases} \tag{9}$$

Although 1D MinMod slopes are appropriate for second–order methods, we have observed that these slopes violate radial symmetry of radially symmetric problems, i.e. the anisotropy of a numerical solution is increased. Numerical examples of this artificial anisotropy are provided in section 4.

3.2 Two–dimensional limiters

The main motivation for genuinely multi–dimensional limiters is to reduce the anisotropy caused by the standard 1D MinMod limiter. At first, we derive an artificial limiter aligned with a diagonal direction to show that most of the numerically observed anisotropy is caused by the limiter itself. Then, we construct novel limiters using different convex combination of these limiters.

3.2.1 Diagonal MinMod limiter

Here we construct a natural analogue of the 1D MinMod limiter rotated by 45 degrees. We start with the calculation of slopes along diagonals, i.e. along the lines

$$e(x,y) = \frac{x+y}{\sqrt{2}} \qquad f(x,y) = \frac{y-x}{\sqrt{2}} \,. \tag{10}$$

In this case, the natural choice of the left and right difference are

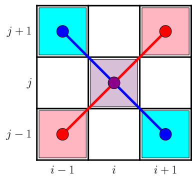

Figure 3: Schematic representation of the limited reconstruction inside the central cell i, j. Potential slopes indicated by ”barbells”. Effective cells emphasized in color.

$$u_{i,j}^{e,L} = \frac{u_{i,j} - u_{i-1,j-1}}{\sqrt{2}\Delta x} \qquad u_{i,j}^{f,L} = \frac{u_{i-1,j+1} - u_{i,j}}{\sqrt{2}\Delta x} \tag{11}$$

$$u_{i,j}^{e,R} = \frac{u_{i+1,j+1} - u_{i,j}}{\sqrt{2}\Delta x} \qquad u_{i,j}^{f,R} = \frac{u_{i,j} - u_{i+1,j-1}}{\sqrt{2}\Delta x} \,. \tag{12}$$

Having these differences, the minmod function (9) is applied to obtain limited diagonal slopes $u_{i,j}^{e}$ and $u_{i,j}^{f}$. Finally, Cartesian slopes are provided by the transformation

$$\frac{\partial u}{\partial x} = \frac{\partial u}{\partial e}\frac{\partial e}{\partial x} + \frac{\partial u}{\partial f}\frac{\partial f}{\partial x} = \frac{1}{\sqrt{2}}\left(\frac{\partial u}{\partial e} + \frac{\partial u}{\partial f}\right) \tag{13}$$

$$\frac{\partial u}{\partial y} = \frac{\partial u}{\partial e}\frac{\partial e}{\partial y} + \frac{\partial u}{\partial f}\frac{\partial f}{\partial y} = \frac{1}{\sqrt{2}}\left(\frac{\partial u}{\partial f} - \frac{\partial u}{\partial e}\right) \tag{14}$$

$$u_{i,j}^{x,\text{MinMod Diag}} = \frac{1}{\sqrt{2}}\left(u_{i,j}^{e} + u_{i,j}^{f}\right) \tag{15}$$

$$u_{i,j}^{y,\text{MinMod Diag}} = \frac{1}{\sqrt{2}}\left(u_{i,j}^{f} - u_{i,j}^{e}\right) \,. \tag{16}$$

3.2.2 Principal and Minor MinMod limiters

The Principal and the Minor MinMod limiters are constructed as a convex combination of the 1D MinMod limiter with the Diagonal MinMod limiter according to the local direction of the unlimited gradient inside each computational cell.

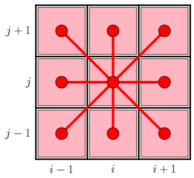

Figure 4: Schematic representation of the limited reconstruction inside the central cell i,j. Potential slopes indicated by "barbells". Effective cells emphasized in color.

Assuming that the direction of the unlimited gradient in a computational cell i,j is given by the polar angle $\Psi_{i,j}$, e.g. $\Psi_{i,j} = \arctan(u_{i,j}^{y,\text{unlim}}/u_{i,j}^{x,\text{unlim}})$ for $x > 0$, we define

$$u_{i,j}^{x,\text{Principal}} = u_{i,j}^{x,\text{1D MinMod}} + \sin^2(2\Psi_{i,j})\left(u_{i,j}^{x,\text{MinMod Diag}} - u_{i,j}^{x,\text{1D MinMod}}\right) \tag{17}$$

$$u_{i,j}^{x,\text{Minor}} = u_{i,j}^{x,\text{1D MinMod}} + \cos^2(2\Psi_{i,j})\left(u_{i,j}^{x,\text{MinMod Diag}} - u_{i,j}^{x,\text{1D MinMod}}\right) \tag{18}$$

and analogically for the y direction.

The function $\sin^2(2\Psi_{i,j})$ reaches local maximum of one along directions of Cartesian axes. Therefore, the 1D MinMod limiter is preferred for the unlimited gradient aligned with Cartesian axes. The function $\cos^2(2\Psi_{i,j})$ in the Minor limiter is shifted by $\pi/4$. The Minor MinMod limiter represents less diffusive alternative to the Principal limiter.

4 NUMERICAL RESULTS

Here we present numerical results using the directional split numerical scheme from section 2 and the various limiters introduced in section 3. We call these results: 1D MinMod, Diagonal MinMod, Principal MinMod and Minor MinMod. Two more results are presented for comparison, namely results of an unlimited method using central differences (Unlimited) for a local gradient approximation and a low–order method with a piecewise constant reconstruction (Donor).

To compare the numerical results, we use the standard $L1$ error

$$E_{L1} = \sum_i \sum_j |u_{i,j}^{t_f} - u_{i,j}^{e}| \Delta x^2 \,,$$

where $u_{i,j}^{t_f} = u^{t_f}(x_{i,j}, y_{i,j})$ denotes numerical solution at the final time t_f and $u_{i,j}^{e} = u^{e}(x_{i,j}, y_{i,j})$ stands for the exact solution and Δx is the mesh spacing.

The $L1$ error is a global measure of a numerical error. It is not a representative measure of radial symmetry (isotropy) violation for the initially radial–symmetric problem. For discontinuous initial data, it is natural to expect some amount of numerical diffusion in the calculated data. In particular, there is no physical reason to introduce any anisotropy for isotropic initial data during linear advection. Standard limiters reduce this diffusion along diagonal directions with respect to square computational mesh. Whereas the $L1$ error is improved through this reduction, we prefer to obtain a mesh–alignment independent solution (even if it is more diffusive). To measure the radial symmetry violation, we replace the exact solution in the $L1$ error by the final numerical solution averaged over angular direction $u_{i,j}^{\text{mean}}$.

The symmetry violation is given by

$$E_s = \sum_i \sum_j |u_{i,j}^{t_f} - u_{i,j}^{\text{mean}}| \Delta x^2 \,. \tag{19}$$

All our test cases in the following are in two dimensions.

4.1 Smooth function advection

The initial smooth Gaussian function $u_{i,j}^0 = \exp(-(5r_{i,j})^2)$ is discretized on the computational domain $(-0.5, 0.5) \times (-0.5, 0.5)$. The advection speed is constant with the advection velocity $(a_1, a_2) = (1, 1)$ for the governing equation

$$\frac{\partial u}{\partial t} + a_1 \frac{\partial u}{\partial x} + a_2 \frac{\partial u}{\partial y} = 0 \,. \tag{20}$$

The $L1$ error of the numerical solution at final time $t_f = 1$ for four different mesh resolutions is presented in Table 1, where the "Donor" method stands for a piecewise constant reconstruction. All limiters show similar error and as well as the order of convergence, which is less than two, as indicated in Table 2.

Grid	Donor	Unlimited	1D MinMod	Diagonal MM	Principal MM	Minor MM
20^2	8.74e-02	9.32e-03	2.86e-02	3.67e-02	3.09e-02	2.93e-02
40^2	5.53e-02	1.58e-03	9.53e-03	1.25e-02	9.78e-03	8.27e-03
80^2	3.21e-02	3.15e-04	3.34e-03	4.32e-03	3.74e-03	2.41e-03
160^2	1.75e-02	7.50e-05	1.01e-03	1.38e-03	1.38e-03	6.85e-04

Table 1: L1 error for four mesh resolutions for the smooth Gaussian function advection.

Grid N/M	Donor	Unlimited	1D MinMod	Diagonal	Principal	Minor
$20^2/40^2$	0.7	2.6	1.6	1.6	1.7	1.8
$40^2/80^2$	0.8	2.3	1.5	1.5	1.4	1.8
$80^2/160^2$	0.9	2.1	1.7	1.6	1.4	1.8

Table 2: Numerical order of convergence, i.e. $\log_2(L1_N/L1_M)$, for the Gaussian function advection.

4.2 Circle advection

Grid	1D MinMod	Diagonal MM	Principal MM	Minor MM
20^2	1.03e-01	1.16e-01	1.11e-01	1.05e-01
40^2	6.62e-02	7.46e-02	7.28e-02	6.81e-02
80^2	4.29e-02	4.83e-02	4.70e-02	4.42e-02
160^2	2.78e-02	3.13e-02	3.04e-02	2.87e-02

Table 3: L1 error for four mesh resolutions for the circle advection.

The circle shape is represented by the initial function $u(r) = 1$ for $r < 0.25$ and $u(r) = 0$ elsewhere, discretized on the computational domain $(-0.5, 0.5)\times(-0.5, 0.5)$ with the advection velocity $(a_1, a_2) = (1, 1)$. The error at final time $t_f = 1$ in L1 norm is presented in Table 3. Initial and advected shapes on a coarse grid are plotted in Figure 5. We can see the artificial anisotropy introduced by the 1D MinMod limiter. As a consequence, initially circular contours become more squared. The same "squaring" is presented for the Diagonal limiter, but the square is now rotated by 45 degrees. It suggests that this anisotropy is caused mainly by the limiter itself, regardless to the error of the directional split update of numerical fluxes. Our proposed Principal and Minor limiters provide more isotropic result.

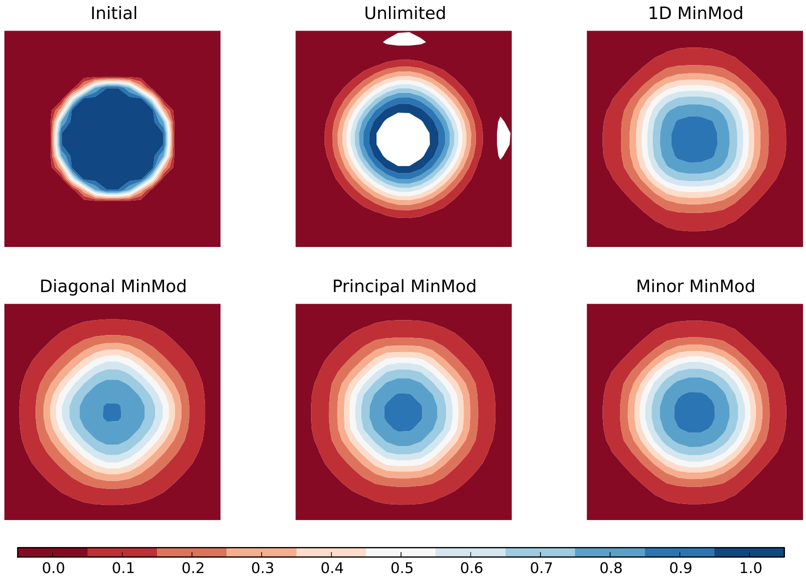

Figure 5: Circle shape contours at the final time 1 with a constant advection velocity (1,1) on a grid size of 20×20 cells for different limiters.

Grid	1D MinMod	Diagonal MM	Principal MM	Minor MM
20	7.31e-03	7.00e-03	4.52e-03	4.37e-03
40	4.36e-03	4.52e-03	3.81e-03	3.52e-03
80	2.84e-03	3.05e-03	2.41e-03	2.78e-03
160	1.55e-03	1.73e-03	1.53e-03	1.62e-03

Table 4: Symmetry violation E_s for four mesh resolutions for the circle shape advection.

In Table 4, the error E_s given by Equation (19) is presented. This error gives a measure of the anisotropy of the limiters. For both the Principal and the Minor limiters, the anisotropy is about two thirds of the 1D limiter for a coarse mesh. This difference is becoming less important with mesh refinement. However, the Principal limiter shows better convergence than the Minor limiter. The convergence with respect to the symmetry violation is shown in Figure 6.

4.3 Hydrodynamic tests

We start the hydrodynamic section with 2D Sedov blast wave followed by 2D Noh implosion test case, showing the importance of an isotropic piecewise linear reconstruction. We compare

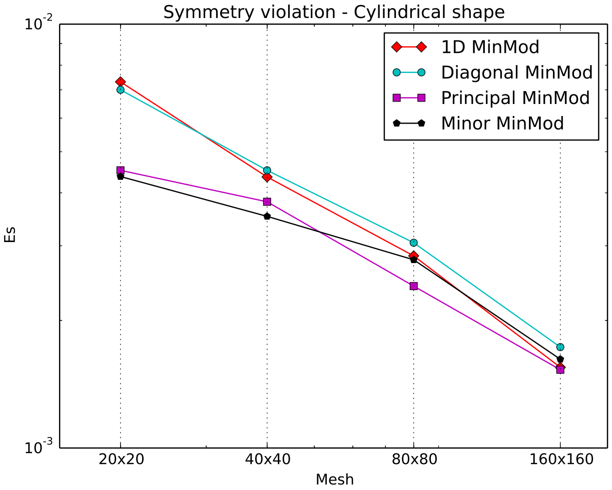

Figure 6: Symmetry violation convergence plots for linear advection of the circle shape for novel limiters.

three different limiters for a piecewise linear reconstruction, which is used in both the predictor step and the Riemann solver state definition.

4.3.1 2D Sedov blast wave

The Cartesian computational domain $(-1.2, 1.2) \times (-1.2, 1.2)$ is covered by a square mesh with 200×200 cells. At the initial time $t = 0$, the fluid (ideal gas with $\gamma = 1.4$) is static and has uniform density $\rho = 1$. Fluid pressure is $p = 10^{-6}$ everywhere except four computational cells in the center of the domain, where $p = 0.0979264/\Delta x^2$, which corresponds to the amount of energy in the definition of Sedov problem [11]. These high–energy cells represent a point initial

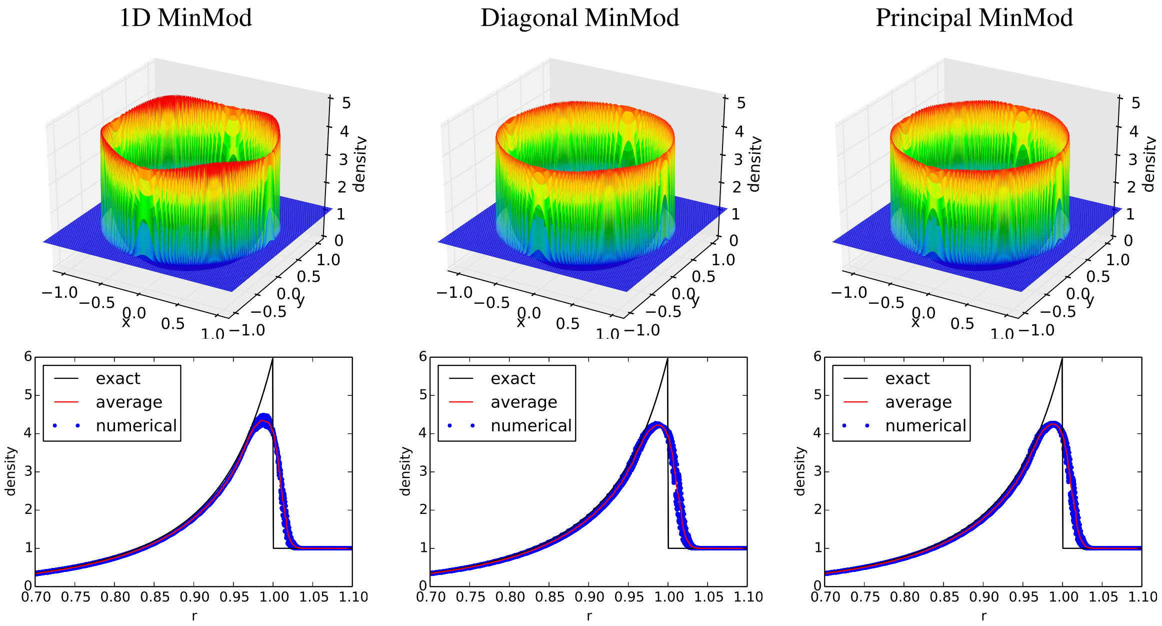

Figure 7: Density surface and scatter plots for Sedov explosion test case. 200 × 200 cells at final time 1.

energy generating a circular shock wave spreading from the center. In the final time $t = 1$, the shock wave reaches the radius $r = 1$. Numerical results are shown in Figure 7.

For the standard 1D MinMod limiter, there is a clear angular dependency of the shock maximal density. The Diagonal limiter is more diffusive along diagonal directions, however it provides a more isotropic solution compared to the 1D MinMod limiter. Overall, the results obtained with the Principal and Diagonal limiters are comparable to each other for this test case and are much more isotropic than the results obtained with the 1D MinMod limiter. The lower part of Figure 7 provides a scatter plot of the final density, where the average solution (in red) is used in the calculation of the symmetry violation (19).

4.3.2 2D Noh implosion

Reduced anisotropy is further demonstrated by results of Noh implosion test case [12] shown in Figure 8 at the final time $t = 0.6$. The computation is initialized with the constant initial density $\rho = 1$ and the radial velocity $u^r = -1$ directed towards the origin on the square domain $(-0.8, 0.8) \times (-0.8, 0.8)$ covered by the equidistant rectangular grid with 200 × 200 cells. The initial and boundary pressure of the fluid with $\gamma = 5/3$ are set to $p = 1 \cdot 10^{-6}$ and we apply the exact density condition on the computational domain boundary $\rho(r, t) = 1 + t/r$ for $r > t/3$.

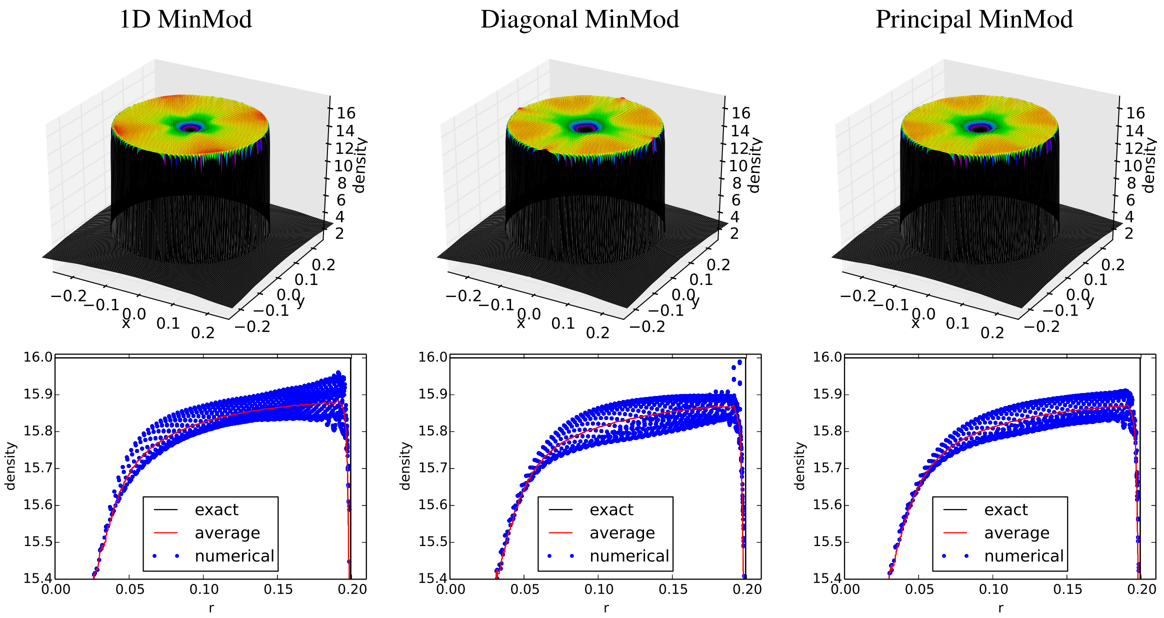

Figure 8: Density surface and scatter plots for Noh implosion test case. 200 × 200 cells at final time 0.6.

According to the construction of the standard 1D MinMod limiter, the numerical diffusion is again lower along the diagonal directions. Consequently, the numerical result is more accurate in regions along the diagonal directions. In Figure 8, these regions are located close to the boundary of the dense central spot with the radius $r < 0.2$, where $\rho^e = 16$. With the Diagonal MinMod limiter the highest–density regions are produced along the directions of the Cartesian axes, whereas with the 1D MinMod limiter, highest–density regions are produced along the diagonal axes, i.e. the regions are shifted by an angle of 45 degrees. In regions of highest–density, results with the Principal MinMod limiter are more diffusive but more isotropic compared to the results with the 1D MinMod limiter. Reduced spread of the density along the central spot is further demonstrated by a zoom in scatter plots in the lower part of Figure 8.

5 CONCLUSIONS

We have demonstrated improved isotropy of the standard one–dimensional slope limiter for a piecewise linear reconstruction on square meshes for a directional split numerical scheme. The anisotropy is reduced by the application of a genuinely multi–dimensional slope limiter. The biggest improvement in the numerical solution calculated by our multi–dimensional minmod limiter (Principal MinMod) is observed on coarse meshes. This multi–dimensional approach could also be extended to other slope limiters. In future work, we will consider estimation of the numerical diffusion in conjunction with estimation of isotropic solution improvements.

ACKNOWLEDGEMENT

This work was performed under the auspices of the National Nuclear Security Administration of the US Department of Energy at Los Alamos National Laboratory under Contract No. DE-AC52-06NA25396. This work is supported by the Advanced Simulation and Computing program under the Hydrodynamics project. LA-UR-16-20072.

REFERENCES

[1] E. F. Toro. *Riemann solvers and numerical methods for fluid dynamics. A practical introduction.* Springer, Berlin, 1999.

[2] A. Kumar. Isotropic finite-differences. *Journal of Computational Physics*, 201:109–118, 2004.

[3] R. K. Shukla and P. Giri. Isotropic finite volume discretization. *Journal of Computational Physics*, 276:252–290, 2014.

[4] K. H. Kim and C. Kim. Accurate, efficient and monotonic numerical methods for multi-dimensional compressible flows Part II: Multi-dimensional limiting process. *Journal of Computational Physics*, 208:570–615, 2005.

[5] J. S. Park and C. Kim. Multi-dimensional limiting process for finite volume methods on unstructured grids. *Computers & Fluids*, 65:8–24, 2012.

[6] T. J. Barth and D. Jespersen. The design and application of upwind schemes on unstructured meshes. Technical Report AIAA-89-0366, NASA Ames Research Center, 1989.

[7] M. E. Hubbard. Multidimensional slope limiters for muscl-type finite volume schemes on unstructured grids. *Journal of Computational Physics*, 155:54–74, 1999.

[8] G. Luttwak and J. Falcovitz. VIP (vector image polygon) multi-dimensional slope limiters for scalar variables. *Computers & Fluids*, 83:90–97, 2013.

[9] B. van Leer. Towards the ultimate conservative difference scheme I. The quest of monotonicity. *Springer lecture notes in Physics*, 18:163–168, 1973.

[10] A. Harten, P.D. Lax, and B. van Leer. On Upstream Differencing and Godunov-Type Schemes for Hyperbolic Conservation Laws. *SIAM Rev.*, 25:35–61, 1983.

[11] L. I. Sedov. *Similarity and Dimensional Methods in Mechanics.* Academic Press, 1959.

[12] W. F. Noh. Errors for calculations of strong shocks using an artificial viscosity and artificial heat flux. *Journal of Computational Physics*, 72:78–120, 1987.